

Design and precision construction of novel magnetic-levitation-based multi-axis nanoscale positioning systems

Won-jong Kim^{*}, Shobhit Verma, Huzefa Shakir

Department of Mechanical Engineering, Texas A&M University, College Station TX 77843, USA

Received 20 July 2006; received in revised form 30 January 2007; accepted 13 February 2007

Available online 12 April 2007

Abstract

This paper presents two novel six-axis magnetic-levitation (maglev) stages capable of nanoscale positioning. These stages have very simple and compact structures, which is advantageous to meet the demanding positioning requirements of next-generation nanomanipulation and nanomanufacturing. Six-axis motion generation is accomplished by the minimum number of actuators and sensors. The first-generation maglev stage, namely the Δ -stage, is capable of generating translation of 300 μm and demonstrates position resolution better than 2 nm root-mean-square (rms). The second-generation maglev stage, namely the Y-stage, is capable of positioning at a resolution better than 3 nm rms over a planar travel range of 5 mm \times 5 mm. A novel actuation scheme was developed for the compact structure of this stage that enables six-axis force generation with just three permanent-magnet pieces. This paper focuses on the design and precision construction of the actuator units, the moving platens, and the stationary base plates. The performance of the two precision positioners is compared in terms of their positioning and load-carrying capabilities and ease of manufacture. Control system design for the two positioners is discussed and an experimental plant transfer function model is presented for the Y-stage. The superiority of the developed instruments is also demonstrated over other prevailing precision positioning systems in terms of the travel range, resolution, and dynamic range. The potential applications of the maglev positioners include semiconductor manufacturing, microfabrication and assembly, nanoscale profiling, and nanoindentation.

© 2007 Elsevier Inc. All rights reserved.

Keywords: Precision assembly; Magnetic levitation; Nanopositioning; Multi-DOF motion control

1. Introduction

In the modern era of nanosystems, the precise manufacture of nanoscale parts is a very crucial task [1]. Precision positioning and vibration isolation play a crucial role while manufacturing, manipulating, or scanning on the micro/nano level. Nanopositioning stages need to meet the demanding positioning requirements of the current and future nanotechnology. These positioning stages along with cutting-edge manufacturing technologies will lead to the development of micro-assemblies and nanostructures. The applications of these stages include microstereolithography (μSTL), nanoscale profiling, and nanoindentation. The key role of a nanopositioning stage is to load, position, and orient an object and keep it stable without much vibration or noise. The stage must be able to travel

in all directions and place the object at the desired position with minimum error. This requires high accuracy, large travel range, and simultaneous generation of multi-DOF (degree-of-freedom) motions and high control bandwidth. However, there are many theoretical and practical challenges in this early phase of nanopositioning and nanomanipulation research. Important technical issues include the development of high-precision manipulation methodologies and the tools for specific applications [2].

Prevailing technologies for ultra-high precision positioning include scanning probe microscopy (SPM). SPM measures and images the object's surfaces on a fine scale, down to the level of molecules and groups of atoms. It is based on the concept of scanning an extremely sharp tip (with a 3–50 nm radius of curvature) across the object surface. The tip is mounted on a flexible cantilever, allowing the tip to follow the surface profile. When the tip moves in proximity to the investigated object, interaction forces between the tip and the surface influence the movement of the cantilever. These movements are detected by selective sensors. By following a raster pattern, the sensor data forms

^{*} Corresponding author. Tel.: +1 979 845 3645; fax: +1 979 862 3989.
E-mail address: wjkim@tamu.edu (W.-j. Kim).

an image of the probe-surface interaction. Three most common SPM techniques are atomic force microscopy (AFM), scanning tunneling microscopy (STM), and near-field scanning optical microscopy (NSOM). Currently most of the atomic-level positioning and profiling is accomplished by AFMs and STMs [3,4]. As an example, the Dimension 3100 SPM of Veeco Instruments utilizes automated AFM and STM techniques to measure surface characteristics for semiconductor wafers, lithography masks, magnetic media, biomaterials, etc. [5]. Although their primary application was topographical imaging, these instruments have become the prime tools for nanomanipulation.

Most of the actuation units in micro/nanopositioning devices are based on piezoelectric materials. Piezoelectric actuators have become a standard solution in precision positioning applications, where the travel range must be small. Zhang and Zhu developed a high-stiffness linear piezoelectric motor with a resolution of 5 nm [6]. This motor is capable of generating a force of 15 N over a travel range of 5 mm with a maximum step size of 3 μm and various motion speeds with precise positioning down to 0.1 μm . Dong et al. presented a 10-DOF nanorobotic manipulator actuated by lead zirconium titanate (PZT) with a linear resolution of 30 nm, rotary resolution of 2 mrad, and speed on the order of several millimeters per second [7]. Among the commercial semiconductor manufacturing equipment companies, Philips and ASML have done significant work with maglev short-stroke stages for lithography. Carter et al. developed a method, apparatus, and system for controlling an electromagnetically levitated reticle-masking blade in a photolithography system [8]. Hollis and Musits suggested mounting a position sensor equipped with planar armature, in operative juxtaposition to a stator, by a spring colonnade basket of flexure columns, which is capable of providing a low-friction precision x - y - θ positioner [9]. Its operations are computer-controlled with feedback of actual position for closed-loop servo operation. Galburt invented an electromagnetic alignment apparatus particularly adapted for use in aligning the wafers in a microlithography system [10].

There are other techniques that have been applied successfully for micromanipulation. Sun et al. fabricated and experimented on a dual-axis electrostatic microactuation system [11]. This actuation system has a 0.01 μm resolution over a planar motion of 5 μm in the x - and y -axes. A high-bandwidth linear actuator consisting of an air-bearing and voice-coil motor was fabricated and tested by Mori et al. [12]. This actuator is capable of 1 nm steps without overshoots or undershoots. Egashira et al. developed a precision stage using a non-resonant-type ultrasonic motor with a resolution of 0.69 nm [13]. Culpepper and Anderson came up with an idea of a low-cost nanomanipulator, which uses a six-axis compliant mechanism driven by electromagnetic actuators [14]. The stage mechanism is monolithic, and its errors are less than 0.2% of the full scale for a cubical volume travel of 100 μm . Zyvex Corporation developed a nanomanipulator that actuates using coarse and fine actuators with 12 mm travel ranges in x , y , and z and provides a resolution better than 5 nm [15].

However, there are several challenges while performing micro/nanomanipulation with most of these technologies. Notable shortcomings of the instruments based on SPM are lim-

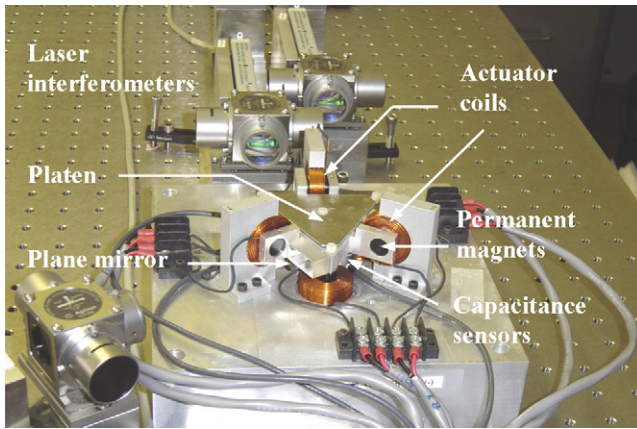
ited number of DOFs and small travel ranges; they are capable of limited manipulation in the x - y plane with a travel range of 100 μm and very small translation (a few micrometers) in the vertical direction with little rotational capability. There are several limitations with piezoelectric actuators as well. They are sensitive to environmental changes such as temperature. Moreover, severe nonlinearities are present in the dynamic behavior of PZT [16]. Well-known phenomena of hysteresis and creep, along with nonlinear voltage dependence affect negatively the dynamic response, sometimes precluding closed-loop operation [17]. Furthermore, the voltage required to operate piezoelectric actuators can be as high as several-hundred volts.

A novel positioning technology is required to overcome the limitations of prevailing techniques discussed above and to fulfill the performance specifications for nanomanipulation and nanofabrication processes. Previous research has shown that magnetic levitation is a promising technology for such applications. Kim and Trumper developed and demonstrated a high-precision planar maglev stage with large planar motion capability which had a 10 nm resolution and 100 Hz control bandwidth [18]. It also eliminated stiction, backlash, and hysteresis that limit the precision in position control. A maglev scanning stage with a 0.6 nm three-sigma horizontal position noise was fabricated and demonstrated by Holmes et al. [19]. The development and motion control of a large travel ultra-precision magnetic-suspension stage was presented by Kuo et al. [20]. Khamesee et al. demonstrated the application of magnetic levitation in a microrobotic system used for the transportation and assembly of miniature parts [21]. This microrobot can be remotely operated in 3 DOFs in an enclosed environment by transmitting magnetic energy and optical signals from outside.

In this paper, we present the design and precision construction of two novel maglev stages for nanoscale positioning. This paper is organized as follows. Section 2 gives a brief overview of the two positioners and compares their benefits with other prevailing precision positioners. Section 3 presents the actuator design and assembly for the two positioners. Design of other key mechanical components, viz. the platens and base plates is discussed in Sections 4 and 5, respectively. Identification of the transfer functions and control system design are presented in Section 6. Following is a summary of the performance of the two positioners and their characterization in the experimental results section, Section 7.

2. Overview of the maglev stages

In this section, we give a brief overview of the two maglev positioners. The developed maglev instruments are compared in terms of their characteristics and performance specifications. A comparison with other prevailing technologies is also given to demonstrate the benefits of magnetic levitation, and in particular, the performance of the positioners we developed. Key applications of these maglev devices include nanoscale positioning and manipulation of micro-assemblies and manufacturing of their parts, microstereolithography, vibration isolation for delicate instrumentation, and microscale rapid prototyping.

Fig. 1. Photograph of the Δ -stage.

2.1. Δ -stage overview

Fig. 1 shows a photograph of the Δ -maglev stage. “ Δ ” refers to the shape of the single-moving levitated platen, which consists of a triangular aluminum part and six single-axis actuators [22]. The compact maglev stage uses the minimum number of actuators required for 6-DOF motion. Each vertical actuator consists of a cylindrical magnet and a coil, and each horizontal actuator consists of two cylindrical magnets and a coil. Prevailing precision positioning devices like STMs and AFMs are able to position in the travel range of 100 μm in 3 DOFs. However, our Δ -maglev stage is capable of motion control in all 6 DOFs with the travel ranges of 300 μm in the x -, y -, and z -translations and 3.5 mrad in the x -, y -, and z -rotations. The position resolution is better than 5 nm with position noise less than 2 nm rms [23–25].

2.2. Y-stage overview

Fig. 2 shows a photograph of the Y-maglev stage. “Y” refers to the shape of the levitated single-moving platen. The Y-stage possesses several competitive advantages over the Δ -stage in terms of travel range, payload capacity, simplicity in mechanical design, and power consumption:

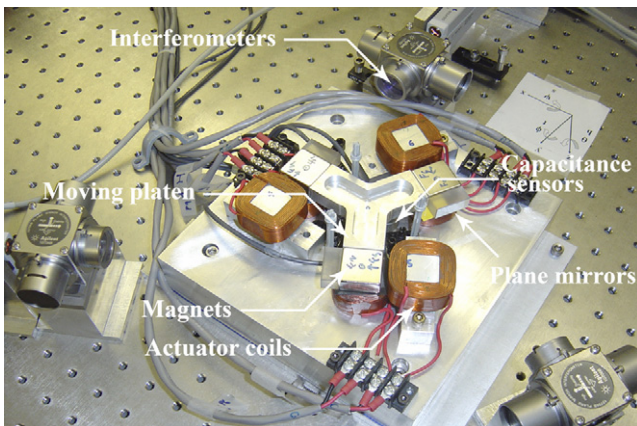


Fig. 2. Photograph of the Y-stage.

Table 1
Comparison with other technologies

Technologies	Travel range (μm)	Resolution (nm)	Dynamic range ($\times 10^3$)
SPM scanner [5]	120 (x, y) 6 (z)	1.83	66
Flexure mechanism [14]	0.1 (x, y, z) 100 (x, y, z)	10 150	0.01 0.67
Δ -Stage	300 (x, y) 300 (z)	2 33	150 9
Y-stage	5000 (x, y) 500 (z)	3 33	1667 15

- Larger travel range:** This second-generation Y-stage has the planar travel range more than 15 times wider (5 mm \times 5 mm) than that of the Δ -stage. Due to sensor specifications, this Y-stage is currently limited to move 500 μm in the z -axis and 0.1° in rotation. However, the mechanical design of the stage makes it capable to rotate about 5° and translate about 7 mm in z with proper sensors.
- Higher payload capacity:** The payload capacity of the Y-stage is 2 kg as compared to 0.3 kg of the Δ -stage.
- Fewer number of parts:** The Y-stage is based on a novel actuation mechanism in which forces in two perpendicular directions are generated by a single magnet (Refer to Section 3.2 for details). This reduced the number of magnets by a factor of three compared with that in the Δ -stage.
- No mechanical restriction:** The platen of the Y-stage can be removed from the stage frame easily without disturbing any stationary parts. This facilitates easy loading and unloading of objects on the platen for various applications, which is an added advantage over the nanomanipulator developed by Culpepper and Anderson [14] and the Δ -stage [23].

Table 1 gives a comparison of the developed maglev stages with two prevailing positioning technologies [5,14] in terms of the travel range, position resolution, and dynamic range (travel range divided by position resolution).

3. Actuator units

3.1. Actuator units for the Δ -stage

3.1.1. Actuator design

The force between the current-carrying coil and the permanent magnet is calculated by the Lorentz law

$$\mathbf{f} = \int (\mathbf{J} \times \mathbf{B}) dV \quad (1)$$

where \mathbf{J} is the current density (A/m^2) in the coil, \mathbf{B} the magnetic flux density (T) generated by the permanent magnet, and dV the small volume segment in the coil. The magnet assembly (described in the following subsection) produces a magnetic field on the concentric current-carrying coil. The magnetic

flux density is related to the magnetic scalar potential Ψ as $\mathbf{B} = -\mu_0 \nabla \Psi$, where Ψ was obtained by the following superposition integral [26] and is given by

$$\Psi = \int \frac{\rho_m(r')}{4\pi\mu_0 |r - r'|} dV' \quad (2)$$

In Eq. (2), ρ_m is the volume magnetic charge density in the magnet, and \mathbf{r} and \mathbf{r}' are the position vectors to an observer on the coil and an infinitesimal volume segment dV' in the magnet, respectively. Then, the resulting force can be found from the triple integral of $\mathbf{J} \times \mathbf{B}$ over the whole coil volume V' . The design calculations were performed using MathCAD. Because of the difficulty in deriving a closed-form expression, we chose to calculate the force with respect to a set of given values of z , and used the “polyfit” command in MATLAB to obtain a gap-dependent current–force relation using least-square polynomial fit. In the operating travel range of 300 μm , however, this force constant essentially remains constant. A detailed explanation of the design calculations was reported in Ref. [24].

3.1.2. Assembly

The six-axis motion generation by the platen for the Δ -stage is achieved by the application of a combination of independent force components acting through six unit actuators. Each horizontal-actuator unit consists of two cylindrical permanent magnets attached together with an aluminum spacer between them placed inside a doughnut-shape current-carrying coil. Each vertical-actuator unit consists of one permanent magnet and a current-carrying coil identical to those in a horizontal-actuator unit. The assembly of the magnets and spacer is attached to the moving platen, while the six current-carrying coils are fixed to the stationary base plate.

Schematics of the assemblies of the horizontal and vertical actuators are shown in Fig. 3. The coil generates the N or S pole based on the direction of the current governed by the right-hand rule. Depending on its magnetization direction, an attractive or repulsive force is applied on the magnet. A magnet-coil air

gap of 0.5 mm limits the total achievable travel range of the platen.

All the magnets and aluminum spacers/mounts were fixed using PC-7 epoxy with an 8 h curing time. The precision tooling was designed and constructed for the assembly of these actuator units. A pocket of a 11.5 mm square with the round corners of a 3.175 mm radius was machined. The height of the tooling for the vertical actuators is 13.513 mm, and for horizontal tooling, 22.987 mm. The surfaces to be fixed were cleaned with methyl ethyl ketone (MEK) and scratched with sandpaper which increased the bonding strength. All the surfaces to be fixed were applied a thin layer of epoxy. Spray of dry-film mold release was applied on the tooling so that the magnets and spacer/mount would not stick to the tooling. Then magnet assemblies were placed in the tooling and were squeezed and held between two flat surfaces with G-shaped clamps. The assemblies were kept for at least 24 h for curing and were then taken off. The pocket sides in the tooling of the exact size ensured a very precise alignment of the magnets and spacer/mount. The preset height of the tooling ensured the uniform epoxy thickness and overall length from one magnet assembly to another.

The primary benefit of this maglev stage apart from its precision positioning and load-carrying capabilities is the nominal power consumption by the actuators. The average nominal current in each vertical actuator is 0.7 A, so the power consumption with the coil resistance of 0.6 Ω is only around 1 W in the entire actuation system to levitate the platen against gravity. Assuming the coils to be point sources of heat, this power consumption would increase the temperature of the base plate by a maximum of 0.2 $^\circ\text{C}$. Furthermore, this heat is transferred to the platen only through convection since there is no mechanical contact between the base plate and the platen. Thus, for all practical purposes, the thermal expansion errors due to heat losses in the positioner that would be detrimental to its nanoscale positioning capabilities may be safely ignored. The characterization of these actuators was described in detail in Ref. [22]. The detailed specifications of the actuating units in the Δ -stage are given in Table 2.

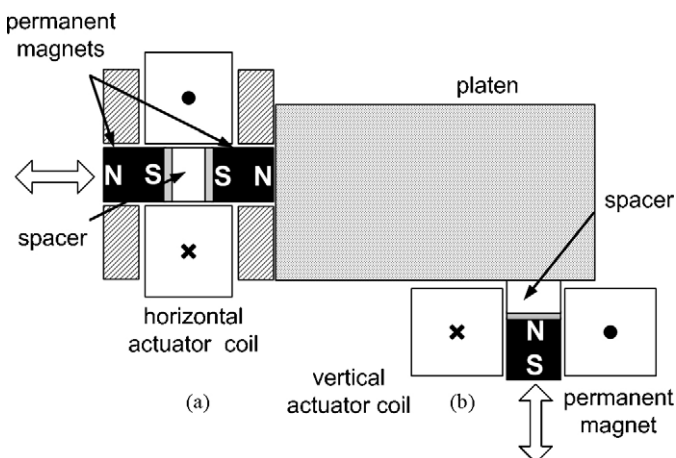


Fig. 3. Schematics of (a) the horizontal-actuator unit and (b) the vertical-actuator unit.

Table 2
Properties of actuators [27]

	Property	Δ -Stage	Y-stage
Permanent magnet	Size (mm)	$\varnothing 11.7$	25.4×25.4
	Height (mm)	9.5	12.7
	Material	NdFeB	NdFeB
	Energy product (kJ/m^3)	400	280
Coil	Wire gauge	AWG#24	AWG#24
	Material	Copper	Copper
	Turns	179	679^{V} ; 561^{H}
	Resistance (Ω)	0.6	5.5^{V} ; 5.9^{H}
	Inner dimension (mm)	$\varnothing 12.2$	$10 \times 10^{\text{V}}$; $20 \times 20^{\text{H}}$
	Outer dimension (mm)	$\varnothing 32.5$	$35 \times 35^{\text{V}}$; $40 \times 40^{\text{H}}$
	Thickness (mm)	9.6	17.5

V: vertical actuator, H: horizontal actuator.

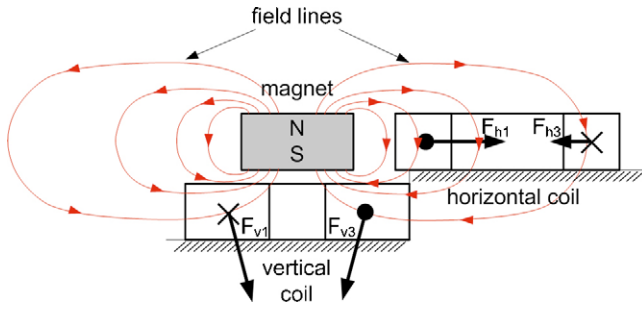


Fig. 4. Cross-sectional side view of the novel two-axis actuator.

3.2. Actuator units for the Y-stage

3.2.1. Actuator design

The working of the Y-stage is based on a novel 2-axis electromagnetic-force generation scheme, which generates forces on a single permanent magnet in two perpendicular directions using two current-carrying horizontal and vertical coils [27]. The terms “vertical coil” and “horizontal coil” are used for the coils to generate vertical and horizontal actuation, respectively. Fig. 4 shows a cross-sectional view of each actuator unit. There are three such units at the three ends of the Y-shaped platen shown in Fig. 2. The magnetic-field lines generated by the permanent magnet are also shown in Fig. 4. The directions of the currents in flow are assumed clockwise in the vertical coil and counterclockwise in the horizontal coil, seen from the top. The maglev stage is comprised of three such actuating units with three permanent magnets attached to ends of the Y-shaped platen and two fixed square-shaped coils per magnet. The magnetic flux generated by the magnet is shared by the two coils, one right below and another on the side of the magnet. The magnitude and directions of currents in the coils govern the forces exerted on the magnet following the Lorentz-force law. In the vertical coil, the direction of the magnetic-field lines is normal to the direction of current flow and towards the center of the coil on all the four sides of the coil (neglecting the corner effect). Thus, the Lorentz force on the coil is vertically downwards on all the four sides of the square. The equal electromagnetic reaction force is applied vertically upwards on the moving magnet since the coil is fixed in a stationary frame. Similarly, in the horizontal coil the direction of the magnetic-field lines is approximately downwards in all the four sides. Thus, the effective force on the coil is to the right following the right-hand rule, and on the magnet, to the left. To change the magnitude and directions of the vertical and horizontal forces, we make appropriate changes in the magnitude and directions of current flow in the corresponding coils. In this manner we can generate the forces in the two perpendicular directions independently on a single-moving magnet. The detailed specifications of the actuating units in the Y-stage are given in Table 2.

The force generated by the interaction between the permanent magnet and the coil current follows the Lorentz force given by Eq. (1). The limits of the integral are set to cover the entire volume of the coil. After substituting the physical parameters of the magnet and the coil, the expression of the force acting on the volume (V) of the coil due to the surface (S) magnetic charge on

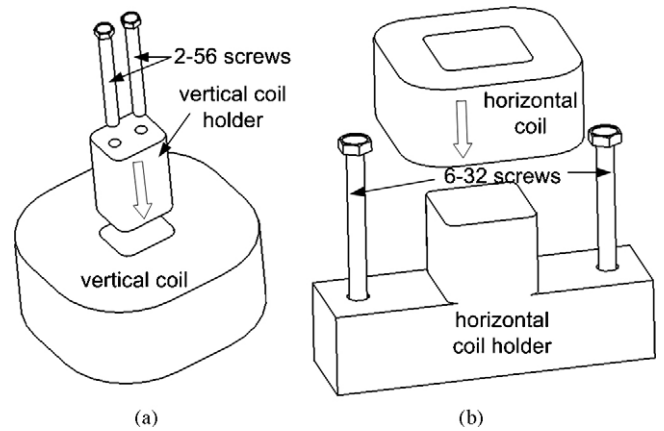


Fig. 5. Exploded views of (a) the vertical-coil and (b) the horizontal-coil assemblies.

the magnet becomes the following quintuple integration.

$$f = \frac{J\sigma_m}{4\pi} \iint_S \left(\iiint_V \frac{-(x-p)\hat{k} + (z-r_1)\hat{i}}{[(x-p)^2 + (y-q)^2 + (z-r_1)^2]^{3/2}} dy dx dz \right) dp dq \quad (3)$$

In the above equation, $\sigma_m = \pm\mu_0 M$ is the surface magnetic charge density on the top and bottom surfaces of the magnet with permanent magnetization M (A/m). The permeability of free space μ_0 is $4\pi \times 10^{-7}$ H/m, and \hat{i} and \hat{k} are the unit vectors in the stationary frame attached to the coil; p , q , and r_1 are the integration variables for distance of the surface element on the magnet from the coordinate origin in the x -, y -, and z -axis, respectively. For the sake of computational simplicity, we made use of the coil symmetry by dividing it in four sections along the diagonals and performed the force calculations with the quintuple integral only on one of them. Details of these design calculations for optimal actuator sizing, its performance at offset points, and experimental verification of the final design values may be found in Ref. [28].

This new actuation scheme has several advantages over the previous one. (1) It makes the mechanical design of the maglev stage very simple to manufacture and assemble, (2) there is no mechanical constraint on the platen to separate it from the actuator assembly, and (3) since there are only three magnets used to generate actuation forces in all the six axes, the structure of the platen is simple. The coils need to be attached to the base plate at precise locations and orientations. The surface of the coils should also match perfectly with the top plane of the base plate. Therefore, we designed and fabricated coil holders shown in Fig. 5 for both the vertical and horizontal coils and fixed them together using assembly fixtures.

3.2.2. Vertical-coil assembly

Attaching the vertical coil to the base plate was somewhat cumbersome because this coil could not be held from the outside and no part of the coil holder can come out of the coil due to its

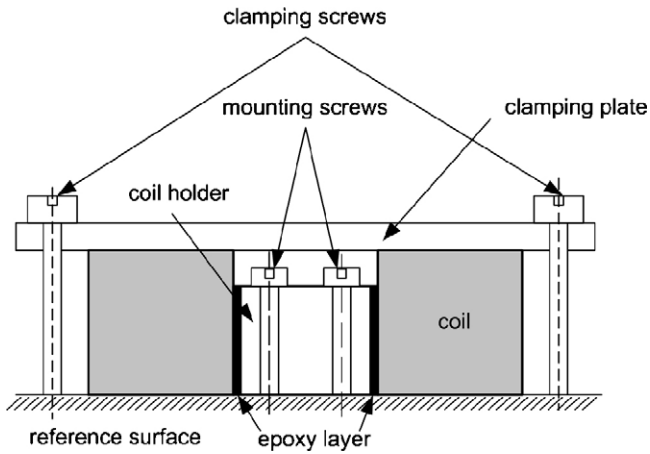


Fig. 6. Fixture to pot the vertical coil to its coil holder.

tight packaging. Thus, we designed the coil holder as an insert in the coil and fixed it inside the coil. An exploded view of the vertical-coil assembly is shown in Fig. 5(a). The coil holder was fabricated to perfectly fit to the inner surface of the vertical coil leaving space for epoxy. It has 2 through holes for the screws so that the coil can be placed at a precise position and orientation. To bond the vertical coil accurately within its holder we designed the assembly fixture shown in Fig. 6. The inner surface of the coil and the outer surface of the coil holder were bonded together with PC-7 epoxy. The reference plate and the clamping plate were coated with dry-film mold release thoroughly. The coil holder was mounted on the reference plate, and then the coil was placed on the top. A clamping plate was used to press the coil from the top. This assembly was kept for 24 h to cure the epoxy.

3.2.3. Horizontal-coil assembly

The horizontal coils needed to be placed at the same horizontal level as that of the platen. An inverted-T-shaped coil holder was designed and fabricated that could hold the horizontal coil from inside and support it from the bottom. An exploded view of the assembly is shown in Fig. 5(b). A fixture similar to the

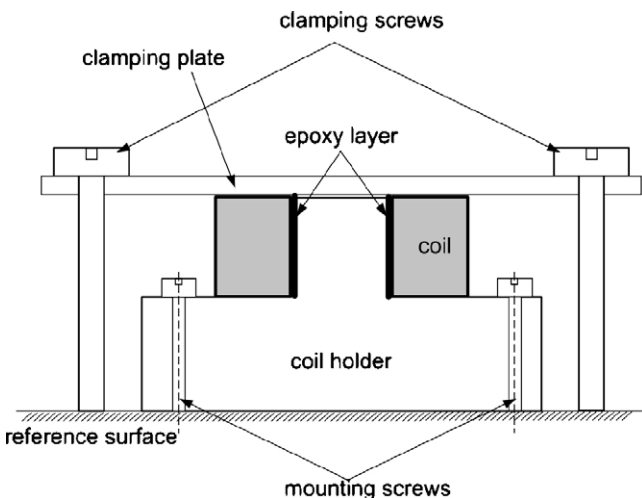


Fig. 7. Fixture to pot the horizontal coil within its coil holder.

one used for the vertical-coil assembly was constructed. The assembly procedure is shown in Fig. 7. The coil and the coil holder were bonded in place with PC-7 epoxy, and the clamping plate was coated with dry-film mold release. Then the coil holder was mounted on the reference plate, and the clamping plate was fastened after the coil was placed.

4. Platen design and assembly

Fig. 8 shows exploded views of the two maglev positioners. The triangular part in the center in Fig. 8(a) and the Y-shaped part in Fig. 8(b) are the single-moving platens. The platens carry permanent magnets for actuation and plane mirrors for horizontal motion sensing. The details of the platen design and precision assembly are described in the following sections.

Effective packaging is important for any assembly. Thus, we designed all parts and their assemblies in SolidWorks® in such a way that (1) the platens must be close enough to all coils for sufficient force generation, (2) the bottom surfaces of the platens must be in the sensing range of all capacitance probes, and (3) the HeNe laser beams from the interferometers should not be blocked.

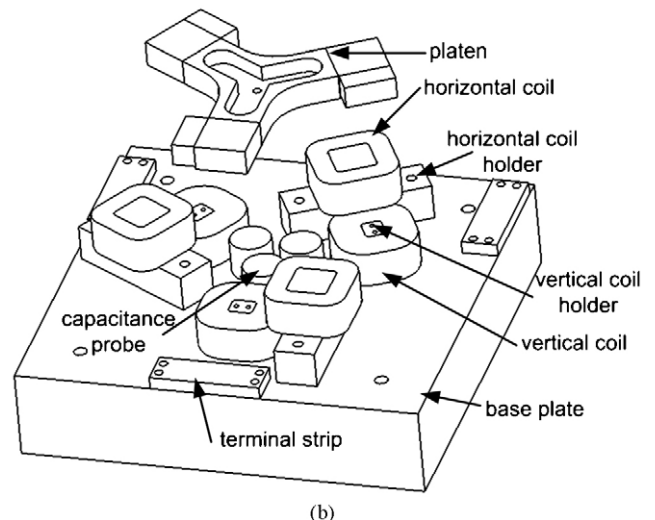
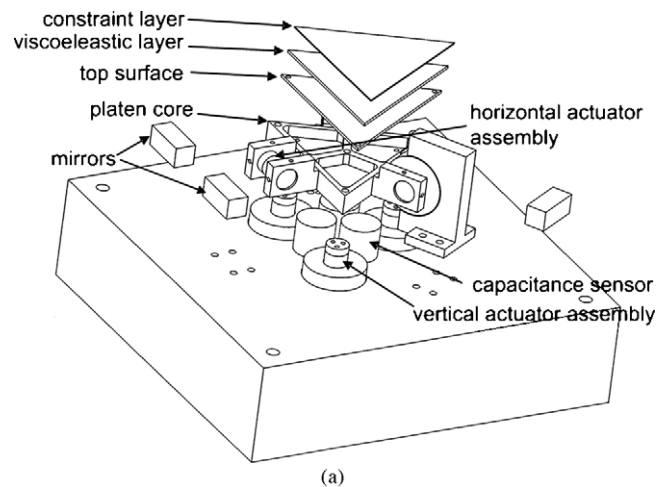


Fig. 8. Exploded views of (a) the Δ -stage and (b) the Y-stage.

Since the platen is the only moving part in each of the whole maglev stages, its design is very crucial with the following considerations: (1) the vertical actuators must continuously apply vertical forces to balance the platen's weight against gravity at a predetermined levitation height, (2) the platen should be light to maintain the coil currents in the actuators low, and (3) the moving and stationary structures should be stiff enough to exhibit a high natural frequency.

4.1. Δ -stage platen

The core of the platen is made of pocket-milled single-piece aluminum to reduce its mass and to keep its natural frequency high without sacrificing stiffness. A finite-element analysis shows the natural frequency of the platen at as high as 4.6 kHz. There is no iron part in the assembly, which makes the actuators operable at high bandwidth without magnetic saturation or hysteresis. The parts attached to it are three horizontal magnet assemblies, three vertical magnet assemblies, three plane mirrors, and a set of aluminum, viscoelastic, and constraint layers on top. The assembly of these three layers adds passive damping to the system to minimize the structural vibrations and improve the stability. The bottommost aluminum layer, called the top plate, covers the pockets of the platen. It was attached to the platen using four screws, three at the corners and the fourth at the center. The total mass of the moving part is 0.212 kg.

The horizontal and vertical actuator assemblies were described in the previous section. There are three pairs of arms protruded on the sides of the platen to hold the magnet assemblies for horizontal actuation. Each arm has a hole with its diameter 10 μm larger than that of the cylindrical magnet. The three setscrews on the outer, top and bottom surfaces of the arm were tightened to hold the magnet. Since the magnetization directions of the magnets are parallel to the sides of the triangular platen, these units generate horizontal force parallel to the sides of the platen. Each of the three vertical actuator assemblies consists of a cylindrical magnet and a cylindrical aluminum mount with three holes potted together. Each assembly is mounted on the platen using three screws.

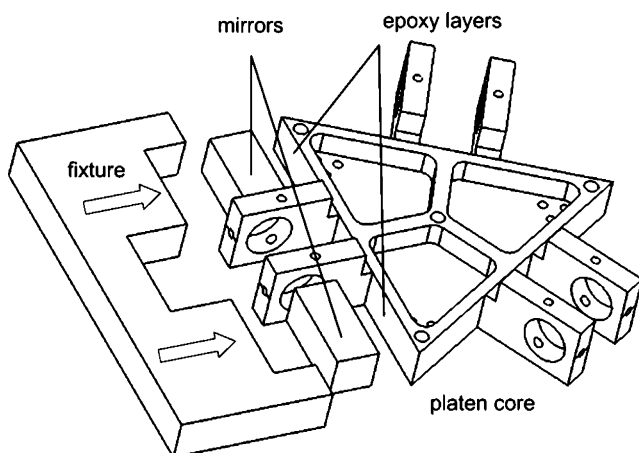


Fig. 9. Tooling used to fix the plane mirrors to the Δ -platen core.

Three plane mirrors for horizontal motion sensing were mounted on the platen using double-sided tape. These plane mirrors act as the reflectors for the laser interferometers. Two of the mirrors are on one side of the platen, and the third, on the second side at an angle of 120° . To ensure satisfactory parallelism of these mirrors a tooling was designed and fabricated. This tooling and the mirror assembly are shown in Fig. 9. The bottom surface of the platen was machined and ground to be flat within $2.54 \mu\text{m}$ as this surface would be used as the targets by the capacitance probes to sense the vertical displacements of the platen.

4.2. Y-stage platen

4.2.1. Platen core

The platen core was machined from single-piece aircraft-grade 7075 aluminum. It was pocket-milled in the center leaving the ribs on the edge to reduce the weight while keeping the high stiffness and natural frequency. The shape of the pocket was decided to make its fabrication easy. The width of the pocket, 15.875 mm, can be machined with a single pass of a 5/8 in.-diameter end-milling tool. Several designs of the platen core with different pocket depths were made and analyzed for the mass and natural frequency. The depth of the pocket was finalized to be 7.62 mm. The three ends of the Y-shaped platen core have a width of 25.4 mm and a height of 12.7 mm to match the side dimension of the magnet. A small hole was drilled and tapped in the center of platen to tighten a screw to hold a grounding wire for the capacitance probes. The bottom surface of the platen was ground to achieve a surface roughness of $2.54 \mu\text{m}$ as this surface would be used as the targets by the capacitance probes.

4.2.2. Assembly

The assembly process of the platen is shown in Fig. 10. The three cuboid-shaped ($25.4 \text{ mm} \times 25.4 \text{ mm} \times 12.7 \text{ mm}$) permanent magnets were attached around the platen core, and then

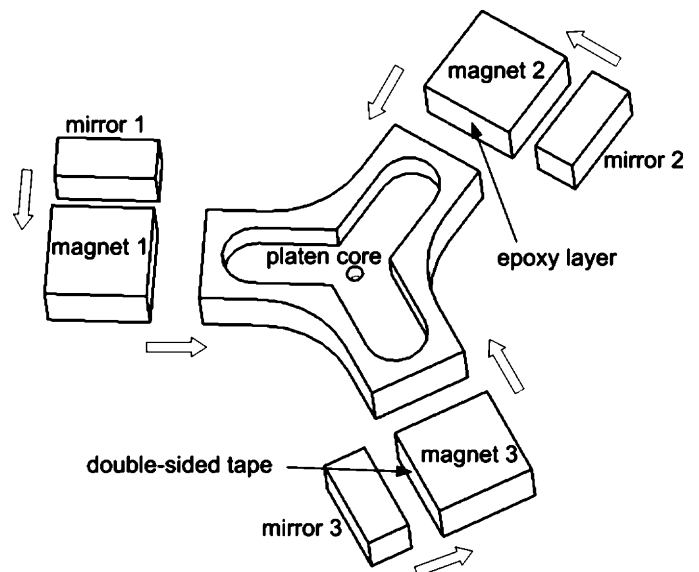


Fig. 10. Assembly of the Y-platen.

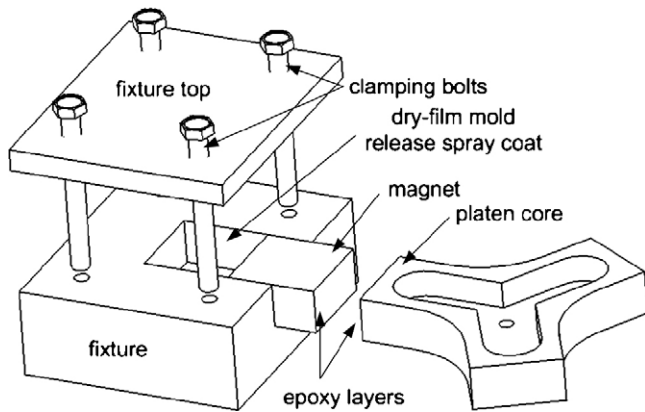


Fig. 11. Fixing process of the magnet with the Y-platen core.

three mirrors were attached at one of the side faces of the magnets. The 25.4 mm square faces on the top and bottom are the N and S poles of the magnets. The faces of the mirrors away from the magnets are the reflecting surfaces.

The fixture shown in Fig. 11 was fabricated and used for precision in the gluing process. Several coatings of dry-film mold release were applied on the fixture so that the magnet or the platen core does not get stuck to the fixture. The magnet face to be bonded and the end of platen core were cleaned with MEK to remove oil and dirt and roughened using sandpaper. A thin layer of PC-7 epoxy was applied on both the surfaces, and the magnet was placed in the fixture. The platen core was inserted from the side and pressed into place. Then the fixture top was clamped with four screws. This assembly was kept for 24 h to provide sufficient time for the epoxy to cure. Then the clamping screws were removed and the assembly was carefully taken off the fixture, and the same procedure was repeated for the two remaining ends.

5. Base plate and stationary assembly

5.1. Δ -stage assembly

The base plate has the dimensions of 203.2 mm \times 203.2 mm \times 56.0 mm. Fig. 12 shows the bottom view of the platen showing the pocket that is milled from the bottom surface of the platen to fasten the screws. All the parts and assemblies were mounted on the base plate via through holes, tapped holes, and pockets. Three screws were used to mount each of the three capacitance probes and fastened from the bottom. There are three circular pockets machined on the top surface of the base plate. The purpose of these pockets was to maintain the heights of the vertical coils at which the vertical magnets will exert the maximum forces when the bottom surface of the platen is in the sensing range of the capacitance probes. Since the radial clearance between the magnets and the coils was just 500 μ m, accurate positioning of the coils was crucial. Thus, a fixture was designed and fabricated to accurately position the coils at the desired locations while we fastened them to the base plate. This fixture had three cylinders mounted on a flat plate as shown in Fig. 13. The diameter of the cylinder was the same as the inner

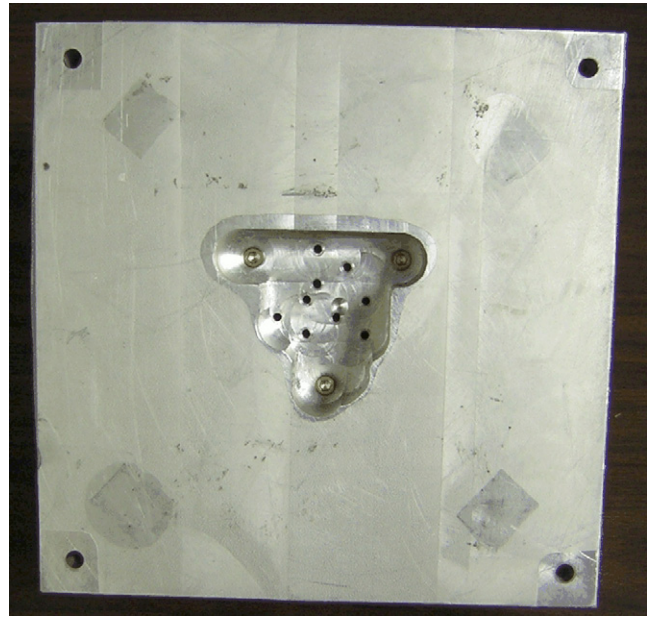


Fig. 12. Photograph of the bottom view of the base plate with nine M3 holes to mount the three capacitance probes. Three additional 10–32 brass screws were inserted to fasten the vertical coils.

diameter of the vertical coils so these cylinders were press fit to the vertical coils. While assembling, the three vertical coils were attached to the fixture and placed on the base plate. Then the three brass screws were tightened from the pocket at the bottom of the base plate. Then, this fixture was slowly taken off. This ensured the position of the coils to be as close as possible to the designed.

The coils for the horizontal actuators were fixed to their coil holders. These coil holders were mounted on the base plate using four screws. Each holder has four through holes, and there are tapped holes on the base plate. Precise alignment of the coils was important while potting because of a low clearance of 504 μ m between the outer diameter of the magnet and inner diameter of the coil, and possible loss of travel range in case of any shift or rotation of the coil. Thus, a fixture was designed and fabricated

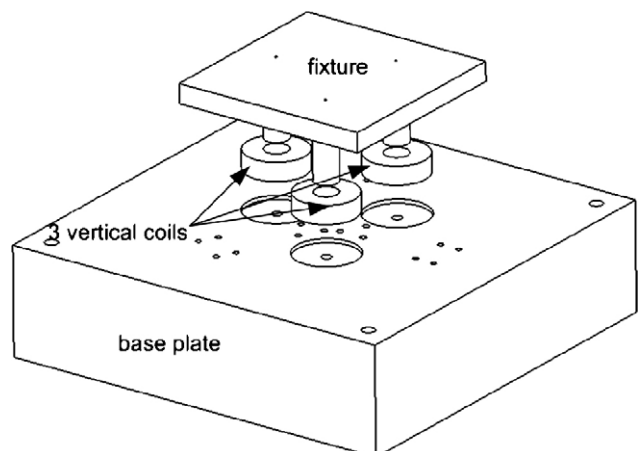


Fig. 13. Tooling for mounting vertical coils to the base plate.

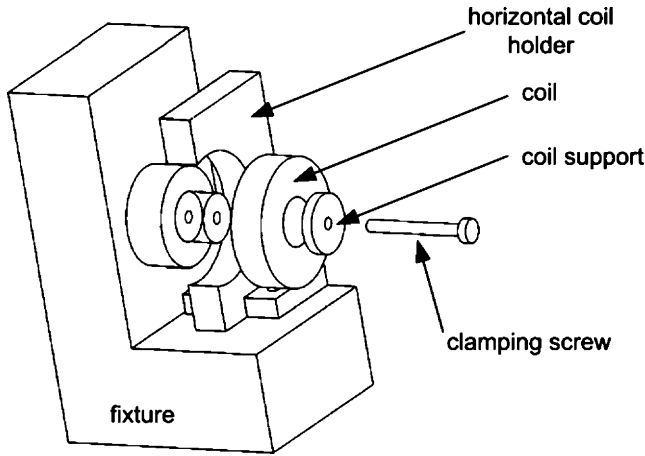


Fig. 14. Tooling to fix the horizontal coil to its coil holder.

for precision assembly. Fig. 14 shows the fixture and the coil holder. The coil holder was mounted on the fixture using the four screws. A cylindrical insert with the diameter the same as the coil inner diameter was used to hold the coil in position. The collar on one side and a supporting disc with a bolt on the other side kept the coil fixed at the desired position relative to the coil holder. A thin film of epoxy was applied on the surfaces of the coil holder and the coil. The coil was held at position for 24 h to cure the epoxy. This process ensured a precise alignment of the coils with respect to the platen with a tolerance of 76 μm (3 mils) by our conservative estimation.

5.2. Y-stage assembly

All the stationary parts are mounted on an aluminum base plate. The three cylindrical pieces placed in the center are capacitance probes. These capacitance sensors were mounted right below the platen at 120°-apart symmetrical positions and measure the height of the platen at three different locations. The

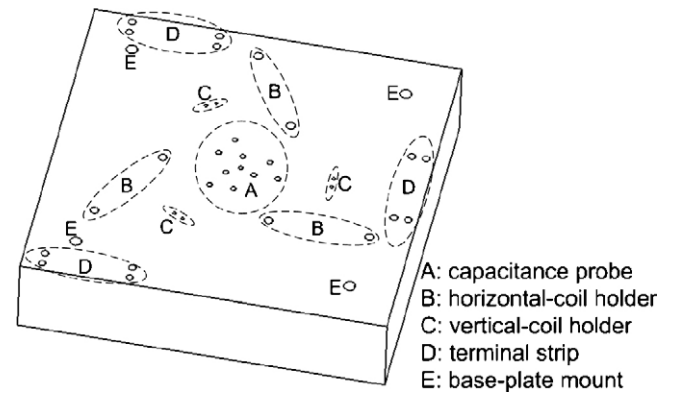


Fig. 15. The base plate for the Y-stage showing the locations of various holes to fix the stationary parts.

vertical-axis motions of the platen are sensed by triangulation of the data gathered from these three capacitance sensors. The vertical-actuator coils were placed adjacent to the capacitance probes. Next to the vertical coils are the horizontal coils mounted with the horizontal-coil holders. Fixed at the edges of the base plate are three terminal strips. Each terminal strip has four contacts to make connections to one vertical and one horizontal coil.

Fig. 15 shows the base plate that holds all the coil assemblies, capacitances probes, and terminal strips. The base plate has an area of 200 mm × 200 mm and a height of 44 mm. The area was designed so that the base plate could hold all the stationary components of the vertical and horizontal actuators and three capacitances gauges. The height was chosen so as to align the plane mirrors on the platen for horizontal motion sensing with the laser beam from the laser head. It was fabricated from solid aluminum to keep its thermal capacity high so that repeated variations in current would not lead to significant thermal-expansion errors. Specific locations of holes for fixing the stationary parts of the assembly are shown in Fig. 15.

Table 3
Summary of maglev-stage specifications

Property	Δ-stage	Y-stage
Moving elements		
DOFs	6	6
Mass (kg)	0.212	0.267
Moment of inertia (10 ⁻⁶ kg m ²)	$\begin{bmatrix} 132.88 & -3.14 & 0 \\ -3.14 & 122.28 & 0 \\ 0 & 0 & 235.87 \end{bmatrix}$	$\begin{bmatrix} 340.37 & 0 & 0 \\ 0 & 340.37 & 0 \\ 0 & 0 & 653.61 \end{bmatrix}$
Size (mm)	80 × 69 × 17.5	115 × 127 × 12.7
Actuation		
Number of coils	6	6
Number of magnets	9	3
Power consumption (W)	1.0	0.8
Motion capabilities		
Travel range (trans.) (mm)	0.3 × 0.3 × 0.5	5 × 5 × 0.5
Travel range (rot.) (mrad)	3.5 × 3.5 × 3.5	3.5 × 3.5 × 3.5
Max acceleration (ms ⁻²)	30	80
Max payload (kg)	0.3	2.0
Position resolution (nm)	5	4
Angular resolution (μrad)	300	100

6. Control

6.1. Controller design

In the absence of any restraining force, the independent plant transfer functions (TFs) for the translational and rotational motions may be respectively represented as

$$\frac{X(s)}{F(s)} = \frac{1}{ms^2} \quad (4)$$

$$\frac{\Theta(s)}{T(s)} = \frac{1}{Is^2} \quad (5)$$

The values of mass m and moments of inertia I for the two positioners are reported in Table 3.

We used the MATLAB function SISOTOOL to select the control parameters. The design method was the same for controllers in all six axes for both the positioners. For the Δ -stage, we set the damping ratio ζ to be 0.7 and the phase margin, 52° at a crossover frequency of 50 Hz. The lead-lag compensator designed for the z -axis motion control for this stage is given by Eq. (6).

$$G_z(s) = \frac{8.7315 \times 10^4 (s + 135)(s + 11)}{s(s + 1385)} \quad (6)$$

The free pole at the origin in the s -plane is to eliminate the steady-state error. We used the same controller for the x - and y -axis motion control. The controllers for the three rotational axes have the same pole-zero locations with the controller gains of 96.872 N, 54.575 N, and 50.221 N for ϕ , ψ and θ , respectively.

For horizontal motion control of the Y-stage, a continuous-time lead-lag controller was designed with phase margin of 69.7° at the crossover frequency of 109.5 Hz. The designed compensator is given by

$$G_{x,y,\phi}(s) = \frac{K(s + 116.6)(s + 10.91)}{s(s + 4014)} \quad (7)$$

where the controller gain K for x and y is 7.3726×10^5 N/m and 1.8041×10^3 N for ϕ .

The design of three SISO controllers for vertical motion control was performed similarly. A continuous-time lead-lag controller was designed to control the vertical motions that has phase margin of 70.1° at crossover frequency of 65 Hz. The compensator is given as

$$G_{z,\psi,\theta}(s) = \frac{K(s + 57.47)(s + 6.271)}{s(s + 2103)} \quad (8)$$

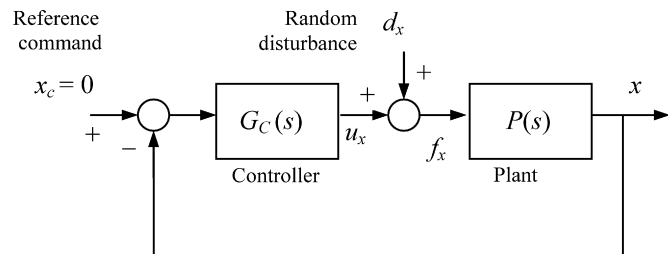


Fig. 16. Block diagram for stochastic transfer function identification.

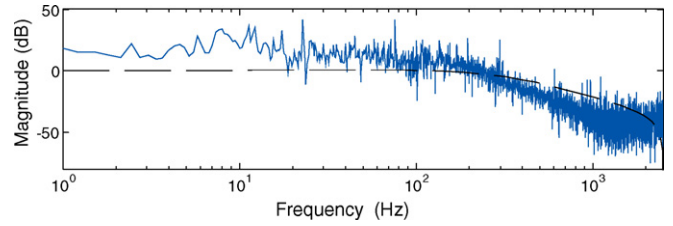


Fig. 17. Closed-loop frequency responses of the analytical model (dashed line) and the plant TFs from the FFTs of the input-output signals (solid line).

The value of K for z is 2.32003×10^5 N/m and 2.95658×10^2 N for θ and ψ .

All the designed controllers were converted to discrete-time difference equations using the zero-order-hold (ZOH) equivalence method with a 5 kHz sampling rate. The control laws were implemented in C on a digital signal processor with the user interface running on VME PC for the real-time control of the positioners.

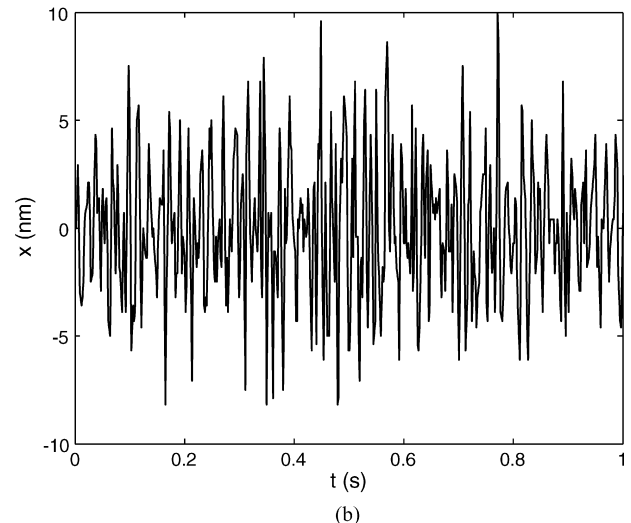
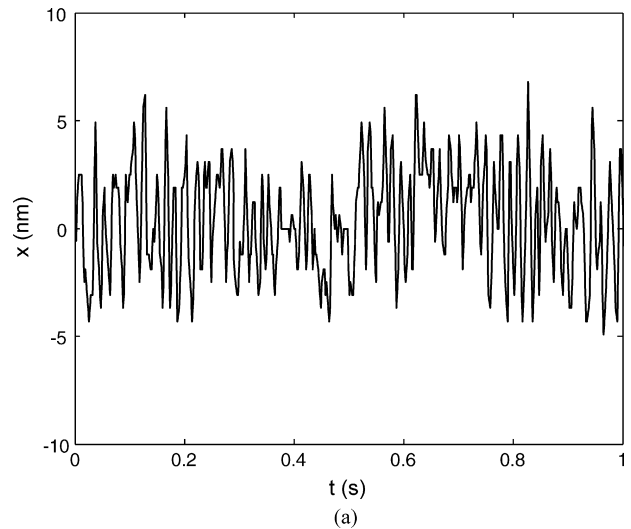


Fig. 18. Position noise in (a) the Δ -stage and (b) the Y-stage.

6.2. Experimental plant TF identification

System identification is necessary in order to verify the analytically determined plant TFs. It is also necessary to analyze and model the plant behavior accurately, to subsequently develop effective controllers. In case of the two maglev positioners reported herein, system identification is particularly challenging because of their open-loop instability. Thus, the system identification needs to be performed in closed loop after the platen is stabilized around the operating point with decoupled lead-lag controllers described in the previous subsection.

Since we have full control over the excitation signal, it is desired to use the signals that persistently excite the plant. Thus, the model validation was performed with a zero-mean, white-Gaussian noise (WGN) as the reference input signal. A detailed treatment of stochastic modeling is covered in classical texts such as [29]. Fig. 16 shows the block diagram to obtain the plant TF. The random disturbance is generated in the software with

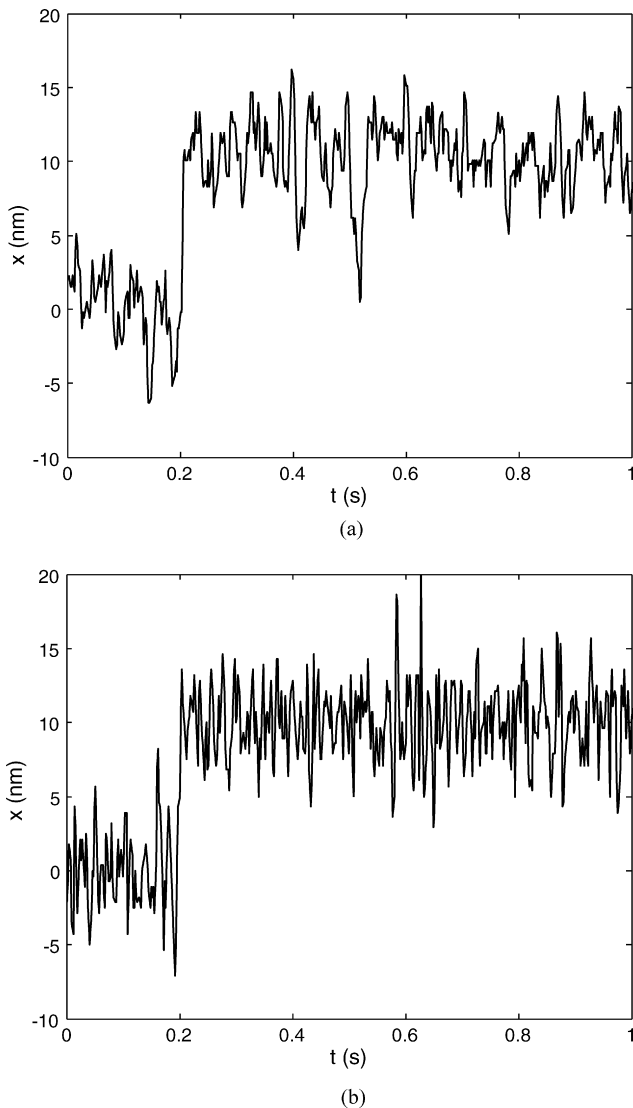


Fig. 19. (a) A 10 nm step response of the Δ -stage and (b) 50 nm step response of the Y-stage.

the “rand ()” function in the C language. The magnitude of the random input signal was increased gradually from 0.1 to 10 μm . These numbers were chosen to excite the plant persistently without losing stability. The total time of the excitation was 2 s with a sampling rate of 5 kHz.

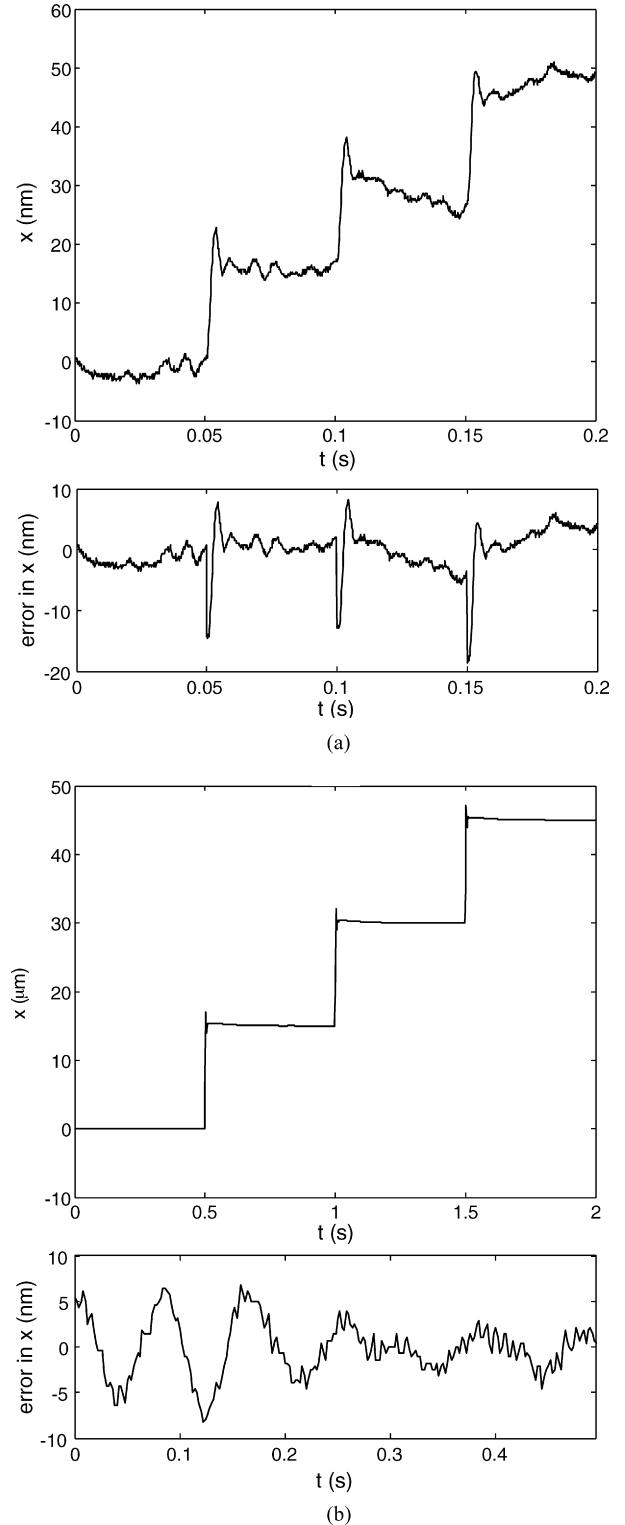


Fig. 20. (a) A 15 nm and (b) 15 μm consecutive steps generated by the Y-stage with command-tracking errors.

The experimental result of the system identification using the input-output time sequences is presented in Fig. 17. The figure shows the analytical closed-loop system response of the Y-stage in the x -axis with the controller given by Eq. (7), and the identified TF. System identification in other five axes was performed in a similar manner. From the figure, it may be noted that the analytical and experimental plant TFs match closely. Therefore, for the rest of the experimental analysis, we have used the analytical plant models Eqs. (4) and (5) for controller design and performance testing.

7. Experimental results

The characteristics and performance specifications of the two maglev stages are summarized in Tables 1 and 3. Sev-

eral experiments were conducted to illustrate the motion-control capability of the maglev stages in terms of position regulation, step responses, and multi-axis contouring. These results have been reported in detail in Ref. [27]. Here we present some of these experimental results to validate the values reported in the tables. These results were taken in the x -axis motion of both the stages as the performance of the y -axis is not much different from that of the x -axis.

The experimental results on the position noise for horizontal motion of the Δ -stage is shown in Fig. 18(a). The position regulation is around 2 nm rms. Fig. 18(b) shows a position noise profile for horizontal motion of the Y-stage, which is better than 3 nm rms. The position noise for the vertical motion is higher due to sensor noise, analog-to-digital conversion (ADC) noise, and ADC quantization. Despite the noise in the vertical axes the hor-

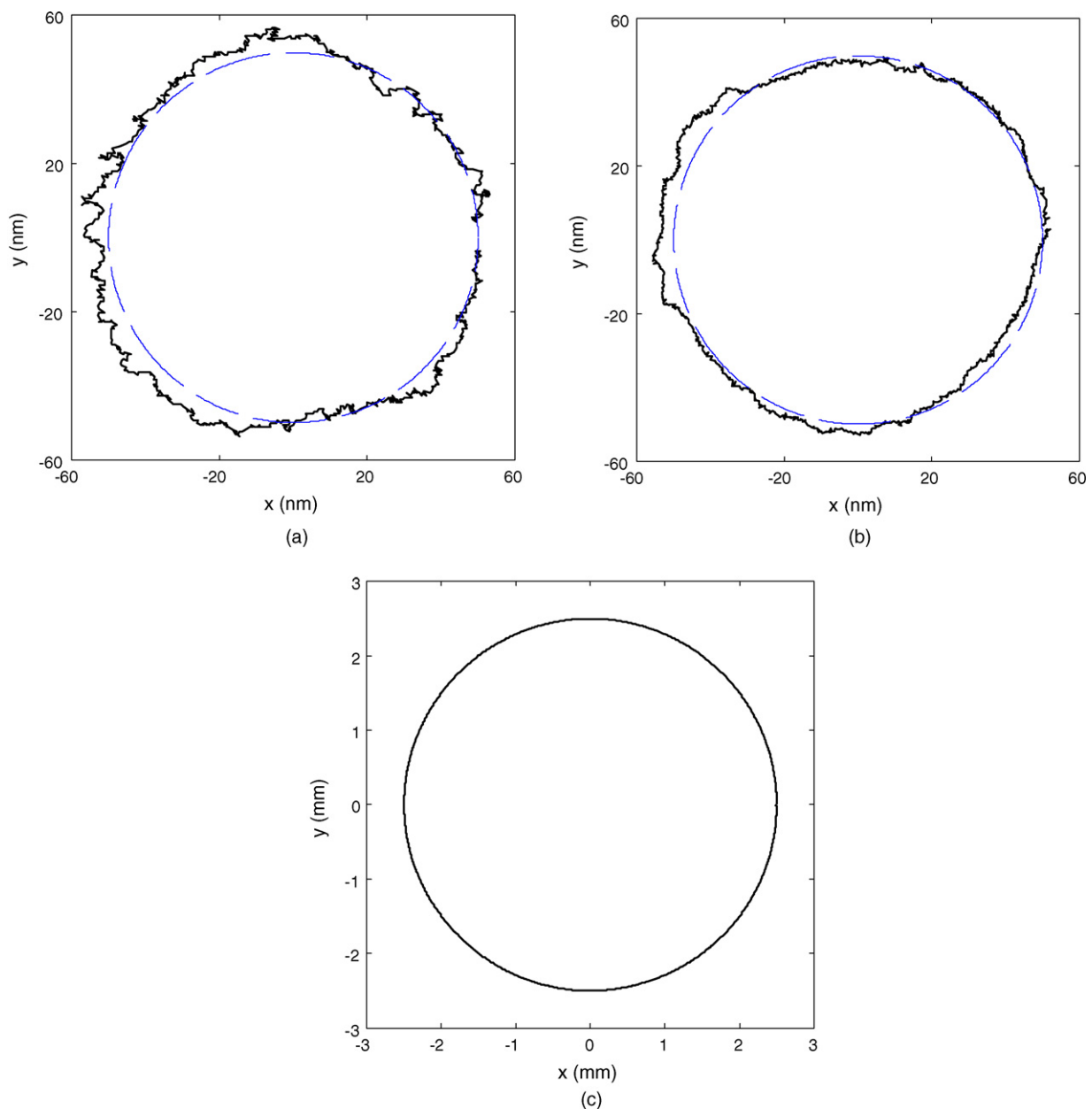


Fig. 21. (a) A 50 nm-radius circle traversed by the Δ -stage, (b) 50 nm-radius circle traversed by the Y-stage, and (c) 2.5 mm-radius circle traversed by the Y-stage.

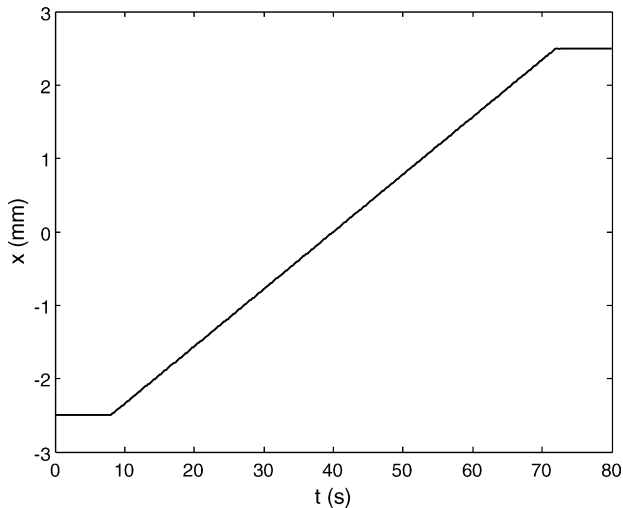


Fig. 22. A 5 mm ramp motion generated by the Y-stage.

horizontal motion profiles are very quiet. This indicates that there is little dynamic coupling between the horizontal and vertical motions of the maglev stages.

Fig. 19(a) and (b) respectively shows a 10-nm step response of the Δ -stage and the Y-stage. The position resolution is clearly better than 5 nm and 4 nm, respectively. Fig. 20 shows experimental results of consecutive steps with the Y-stage. The step sizes are 15 nm and 15 μ m, respectively. The error plots show that even with the scaling by a factor of 1000, the command-tracking errors were within ± 10 nm in both cases.

In the real-time control code written in the C language as an interrupt service routine (ISR), a set of data points in more than one axis can be allocated with respect to time so that the platen can follow a multi-axis trajectory. In Fig. 21(a), a commanded path of a 50 nm-radius circle and the response of the Δ -stage are shown. Fig. 21(b) shows a 50 nm circle traced by the Y-platen. Fig. 21(c) shows a 2.5 mm-radius circular path traversed by the Y-stage in the x - y plane. The motions of the platens were very close to the perfect circles with command-tracking errors within ± 10 nm. These test results demonstrate that the maglev devices can track small multi-axis trajectories and achieve position control at nanoscale precision. It also demonstrates that for the Y-stage with a larger travel range, the positioning capabilities are equally good at micro as well as nanoscale.

The large travel range of the Y-stage has also been demonstrated by a ramp response of 5 mm in the x -axis as shown in Fig. 22. The platen covered the entire travel range of 5 mm from end to end.

8. Conclusions

Precision in nanomanipulation has become the key to the development of the next-generation of nanotechnology. The demands of ultra-high-precision positioning stages are continuously increasing. Currently available stages are able to provide good resolution but over very short travel ranges on the order of several 100 μ m. This limitation will significantly affect the nanoassembly processes when the process needs to be completed

by several different tools. Moreover, prevailing stages have no or very small vertical translation capabilities, which limits their use in micromanufacturing processes. The current nanotechnology requires nanomanipulation stages that can move and position the specimen to various locations and in desired orientations. This motion needs to be in multiple DOFs with long travel ranges at nanoscale resolution.

This paper presented two novel maglev stages that fulfill all the requirements mentioned above. Particular attention was given to the design and precision construction of the actuators and other mechanical components. Additionally, the control system design and experimental results demonstrating the nanopositioning capabilities of the two positioners were also presented. These maglev stages have very simple mechanical structures with a single-moving part, which is easy and inexpensive to fabricate. The constituting components have no mechanical contact between the moving and stationary parts, which facilitates the maintenance of high position resolution. This also eliminates wear in the mechanical parts thereby increasing their life spans and eliminating the requirement of lubricants. Thus, the maglev stages presented in this paper can be used in the nanomanipulation and nanomanufacturing in the next-generation nanotechnology.

Acknowledgment

This material is based on the work supported by the National Science foundation under the Grant No. CMS-0116642.

References

- [1] U.S. Department of Energy. Nanoscale science, engineering and technology research directions.
- [2] Sitti M. Survey of nanomanipulation systems. In: Proceedings of the IEEE conference on nanotechnology. 2001. p. 75–80.
- [3] Bauer C, Bugacov A, Koel BE, Madhukar A, Montoya N, Ramachandran TR, et al. Nanoparticle manipulation by mechanical pushing: underlying phenomena and real-time monitoring. *Nanotechnology* 1998;9(4):360–4.
- [4] Yu MF, Dyer MJ, Rohrs HW, Lu XK, Ausman KD, Her JV, et al. Three-dimensional manipulation of carbon nanotubes under a scanning electron microscope. *Nanotechnology* 1999;10(3):244–52.
- [5] Veeco Instruments. Applications of AFM. <http://web.mit.edu/cortiz/www/nanomechanics.html>.
- [6] Zhang B, Zhu Z. Developing a linear piezomotor with nanometer resolution and high stiffness. *IEEE/ASME Trans Mechatron* 1997;2(1):22–9.
- [7] Dong L, Arai F, Fukuda T. 3D nanorobotic manipulation of nano-order objects inside SEM. In: Proceedings of 2000 international symposium on micromechanics and human science. 2000. p. 151–6.
- [8] Carter FM, Galburt DN, Roux S. Magnetically levitated and driven reticle-mask stage mechanism having six degrees freedom of motion. US Patent 6,906,789; 2005.
- [9] Hollis RL, Musits BL. Electromagnetic X-Y-Theta precision positioner. US Patent 4,514,674; 1985.
- [10] Galburt D. Electro-magnetic apparatus. US Patent 4,506,204; 1985.
- [11] Sun Y, Piyabongkarn D, Sezen A, Nelson BJ, Rajamani R, Schoch R, et al. A novel dual-axis electrostatic microactuation system for macromanipulation. In: Proceedings of IEEE/RSJ international conference on intelligent robots and systems. 2002. p. 1796–801.
- [12] Mori S, Hoshino T, Obinata G, Ouchi K. Linear actuator with air bearing for highly precise tracking [HDD]. In: Digest of the Asia-Pacific magnetic recording conference. 2002. p. AP4-01-2.

- [13] Egashira Y, Kosaka K, Takada S, Iwabuchi T, Baba T, Moriyama S, et al. 0.69 nm resolution ultrasonic motor for large stroke precision stage. In: Proceedings of IEEE-NANO. 2001. p. 397–402.
- [14] Culpepper ML, Anderson G. Design of a low-cost nanomanipulator which utilizes a monolithic, spatial compliant mechanism. *Precis Eng* 2004;28(4):469–82.
- [15] Zyvox Corporation. Zyvox F100 specifications and picture. http://www.zyvox.com/Products/F100_Features.html#.
- [16] Richter H, Misawa E, Lucca D, Lu H. Modeling nonlinear behavior in a piezoelectric actuator. *Precis Eng* 2001;25(2):128–37.
- [17] Requicha AAG, Meltzer S, Terán AFP, Makaliwe JH, Sikén H, Hsieh S, et al. Manipulation of nanoscale components with the AFM: principles and applications. In: Proceedings of IEEE conference on Nanotechnology. 2001. p. 81–6.
- [18] Kim WJ, Trumper DL. High-precision magnetic levitation stage for photolithography. *Precis Eng* 1998;22(2):66–77.
- [19] Holmes M, Hocken R, Trumper DL. The long-range scanning stage: a novel platform for scanned-probe microscopy. *Precis Eng* 2000;24(3):191–209.
- [20] Kuo SK, Shan X, Menq CH. Large travel ultra precision x - y - θ motion control of a magnetic-suspension stage. *IEEE/ASME Trans Mechatron* 2003;8(3):334–41.
- [21] Khamesee MB, Kato N, Nomura Y, Nakamura T. Design and control of a microrobotic system using magnetic levitation. *IEEE/ASME Trans Mechatron* 2002;7(1):1–13.
- [22] Kim WJ, Maheshwari H. High-precision control of a maglev linear actuator with nanopositioning capability. In: Proceedings of American control conference. 2002. p. 4279–84.
- [23] Verma S, Kim WJ, Gu J. 6-axis nanopositioning device with precision magnetic levitation technology. *IEEE/ASME Trans Mechatron* 2004;9(2):384–91.
- [24] Gu J, Kim WJ, Verma S. Nanoscale motion control with a compact minimum-actuator magnetic levitator. *ASME J Dyn Syst Meas Control* 2005;127(3):433–42.
- [25] Verma S, Kim WJ, Shakir H. Multi-axis maglev nanopositioner for precision manufacturing and manipulation applications. *IEEE Trans Ind Appl* 2005;41(5):1159–67.
- [26] Haus HA, Melcher JR. Electromagnetic fields and energy. Prentice-Hall, Inc.; 1989.
- [27] Verma S. Development of novel high-performance six-axis magnetically levitated instruments for nanoscale applications. PhD Dissertation. College Station, TX: Dept. of Mech. Eng., Texas A&M University; 2005.
- [28] Verma S, Shakir H, Kim WJ. Novel electromagnetic actuation scheme for multi-axis nanopositioning. *IEEE Trans Magnetics* 2006;42(8):2052–62.
- [29] Ljung L, Soderstrom T. Theory and practice of recursive identification. MIT Press; 1983.